PROCEEDINGS A

royalsocietypublishing.org/journal/rspa

Research

Cite this article: Dang X, Paulino GH. 2024 Axisymmetric blockfold origami: a non-flat-foldable Miura variant with self-locking mechanisms and enhanced stiffness. *Proc. R. Soc. A* **480**: 20230956. https://doi.org/10.1098/rspa.2023.0956

Received: 23 December 2023
Accepted: 4 March 2024

Subject Areas:
geometry, structural engineering, mechanical engineering

Keywords:
axisymmetric blockfold origami, Miura-ori, non-flat-foldable, self-locking, stiffness

Author for correspondence:
Glaucio H. Paulino
e-mail: gpaulino@princeton.edu

Electronic supplementary material is available online at https://doi.org/10.6084/m9.figshare.c.7132041.

THE ROYAL SOCIETY PUBLISHING

Axisymmetric blockfold origami: a non-flat-foldable Miura variant with self-locking mechanisms and enhanced stiffness

Xiangxin Dang[1] and Glaucio H. Paulino[1,2]

[1]Department of Civil and Environmental Engineering, and [2]Princeton Materials Institute (PMI), Princeton University, Princeton, NJ 08544, USA

XD, 0000-0003-0737-9597; GHP, 0000-0002-3493-6857

Origami foldcores, especially the blockfold cores, have emerged as promising components of high-performance sandwich composites. Inspired by the blockfold origami, we propose the axisymmetric blockfold origami (ABO), which is composed of both rectangular and trapezoidal panels. The ABO inherits the non-flat-foldability of the blockfold origami, and furthermore, displays self-locking mechanisms and enhanced stiffness. The geometry and folding kinematics of the ABO are formulated with respect to the geometric parameters and the folding angle of the assembly. The mathematical conditions are derived for the existence of self-locking mechanisms. We perform compression test simulations to demonstrate enhanced stiffness and increased load-bearing capacity. We find that the existence of rectangular panels not only dominates the non-flat-foldability of the ABO, but also contributes to the enhancement of the stiffness. Our results suggest the potential applications of the ABO for building load-bearing structures with rotational symmetry. Moreover, we discuss the prospects of designing tightly assembled multi-layered origami structures with prestress induced by the mismatch of successive layers to enlighten future research.

1. Introduction

Sandwich structures are extensively used in structural engineering from bridges on the land to aircrafts in the air [1,2]. A sandwich structure is composed of two high-strength outer skins and a low-density inner core placed between them. Classical sandwich cores include numerous members including wood cores, foam cores, honeycomb cores, corrugated cores, textile cores, etc [3]. For aircraft manufacturing applications such as fuselages and wings, only honeycomb cores and a limited number of foams are used due to certification restrictions [4]. However, the honeycomb cores on fuselages create difficulties in venting and do not allow air to escape from the closed cells bounded by the cores and skins. The air can easily condense into water because of the discrepancy of the environments inside and outside the cabin [5]. The condensing water will decrease the structure life and increase weight, especially when it accumulates in the closed cells to a considerable extent. To solve this problem, foldcores were proposed as a replacement of honeycomb cores, dating back to 1960 for the first patent [6] and 1972 for the first publication [7]. As a new type of structural sandwich core, the foldcores were inspired by the concept of origami and have common benefits with honeycomb cores in multifunctional aspects such as the high strength and stiffness-to-weight ratios, good thermal insulation, and acoustic damping. In addition, foldcores allow air flow through their open channels between the skins, and thus avoid moisture accumulation [8,9]. Since the mid-1990s, foldcores have been drawing increasing research interest and a comprehensive review can be found in [10]. One of the most comprehensive studies on foldcores was conducted within the European Union research project CELPACT (Cellular Structures for Impact Performance) [11]. Beyond the zig-zag configurations of Miura origami, the foldcores proposed in CELPACT have additional cell walls at front folding edges and can form blocked configurations when the cores are fully folded in geometry [12,13]. From the viewpoint of origami, the blocked foldcores are distinguished from the Miura foldcores in the sense that the Miura foldcores are flat-foldable while blocked foldcores are not. Therefore, the blocked foldcores essentially correspond to a different class of origami from the classical Miura origami. We refer to this class of origami as *blockfold origami*, to reflect the feature that they can be fully folded to blocked configurations. The sandwich structures with blocked foldcores were shown to have promising performance in both static and impact tests [10]. Naturally, it is intriguing to explore the variations of blockfold origami for potential engineering applications.

The Miura origami has stood out as a highly acclaimed design, since it originated as a solution for packaging and deploying large spatial membranes in 1985 [14]. The unique combination of flexibility and structural integrity makes Miura folds a promising choice in diverse engineering scenarios from reconfigurable architecture [15] and soft robotics [16,17] to electronic devices [18,19] as well as the foldcores in sandwich structures [20,21]. As shown in figure 1*a*, the Miura crease pattern is a tessellation in bi-direction translational symmetry and the repetitive unit cell consists of four congruent parallelograms. Expanding upon the original Miura origami, a spectrum of Miura-derivative patterns have been proposed, including but not limited to cylindrical patterns [22,23], axisymmetric patterns [23–25], and isomorphic/non-isomorphic symmetric patterns [26,27]. These Miura-derivative patterns inherit the topological mountain-valley assignment and geometrical flat-foldable kinematics from the original Miura origami. Additionally, certain Miura-derivative patterns break the original crease topology and flat-foldability to offer distinguished mechanical properties, such as the curved-crease pattern for stacked metamaterials with infinite bulk moduli [28,29] and the blockfold pattern for sandwich structures with high stiffness-to-weight ratios [12,13]. Figure 1*b* demonstrates the crease pattern and folded configuration of a blockfold origami. The blockfold pattern can be obtained by inserting square (or generally rectangular) arrays between rows of the Miura origami. In the Miura pattern, the horizontal mountain and valley creases are arranged alternatively in the vertical direction. By comparison, in the blockfold pattern, the alternative arrangement turns from the single-mountain-single-valley order into the dual-mountain-dual-valley order as a result of the insertion of square cells. The inclusion of square cells also renders

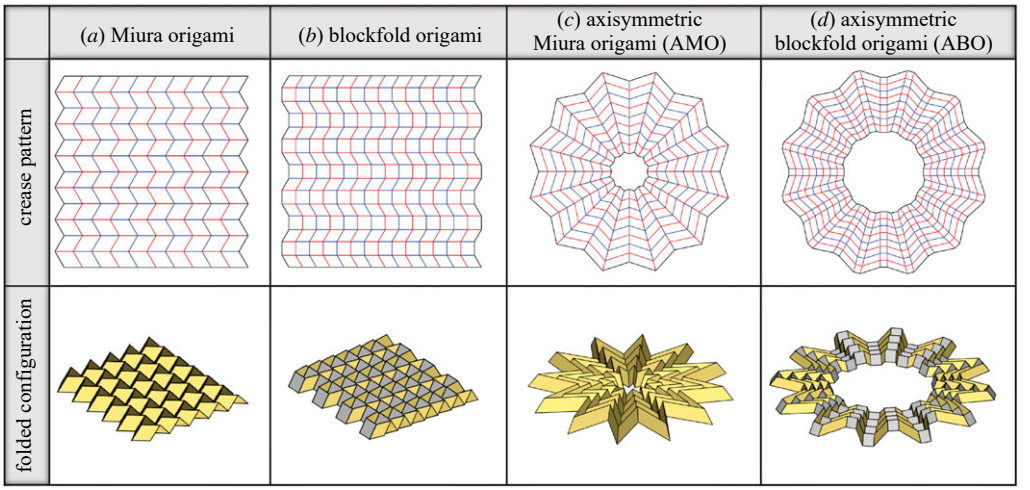

Figure 1. The crease patterns and folded configurations of (*a*) Miura origami, (*b*) blockfold origami, (*c*) axisymmetric Miura origami and (*d*) axisymmetric blockfold origami. The mountain and valley creases are coloured in red and blue, respectively.

the blockfold origami non-flat-foldable with blocked configurations when fully folded. From a different perspective, some Miura-derivative patterns break the translational symmetry of the original Miura pattern, showing distinct folding shapes. A typical example is the axisymmetric Miura origami (AMO) [25] characterized by its rotational symmetry. Figure 1*c* illustrates the crease pattern and folded configuration of an AMO. Compared to the original Miura pattern, parallelograms are modified into trapezoids while the mountain-valley assignment is preserved. The folded AMO takes on a closed-ring shape, and therefore opens up diverse possibilities to design shell structures and stacked metamaterials with rotational symmetry. The AMO is also set apart by its non-monotonic deployment kinematics (i.e. the non-monotonic variation of central angle upon deployment) from Miura variants with translational symmetry [25]. The AMO and the blockfold origami are typical examples of Miura variants that exhibit diverse attributes—rotational symmetry in the former and non-flat-foldability in the latter.

In this paper, we aim to develop a new class of Miura-derivative pattern, the *axisymmetric blockfold origami* (ABO) that features both rotational symmetry and non-flat-foldability. As shown in figure 1*d*, the ABO can be generated by inserting rectangle arrays along the radial direction of the AMO. This paper is organized as follows. In §2, we formulate the geometry of flat patterns and three-dimensional configurations of ABO. We discuss the non-flat-foldability of ABO based on the three-dimensional geometry formulations. In §3, we formulate the folding kinematics of ABO. We discuss the closability and the self-locking mechanisms of ABO based on the folding kinematics formulations. In §4, we show quasi-static compression test simulations of ABO and discuss their enhanced stiffness. In §5, we discuss the prospects of designing tightly stacked axisymmetric origami structures based on the ABO and the AMO. Section 6 concludes the paper.

2. Geometry and non-flat-foldability of axisymmetric blockfold origami

(a) Flat geometry

We start by investigating the flat ABO pattern. As shown in figure 2*a*, we extract the innermost unit cell to describe the geometry of the flat ABO pattern. The unit cell is composed of four obtuse trapezoids and four rectangles. All the trapezoids have two acute angles α and β and two legs b

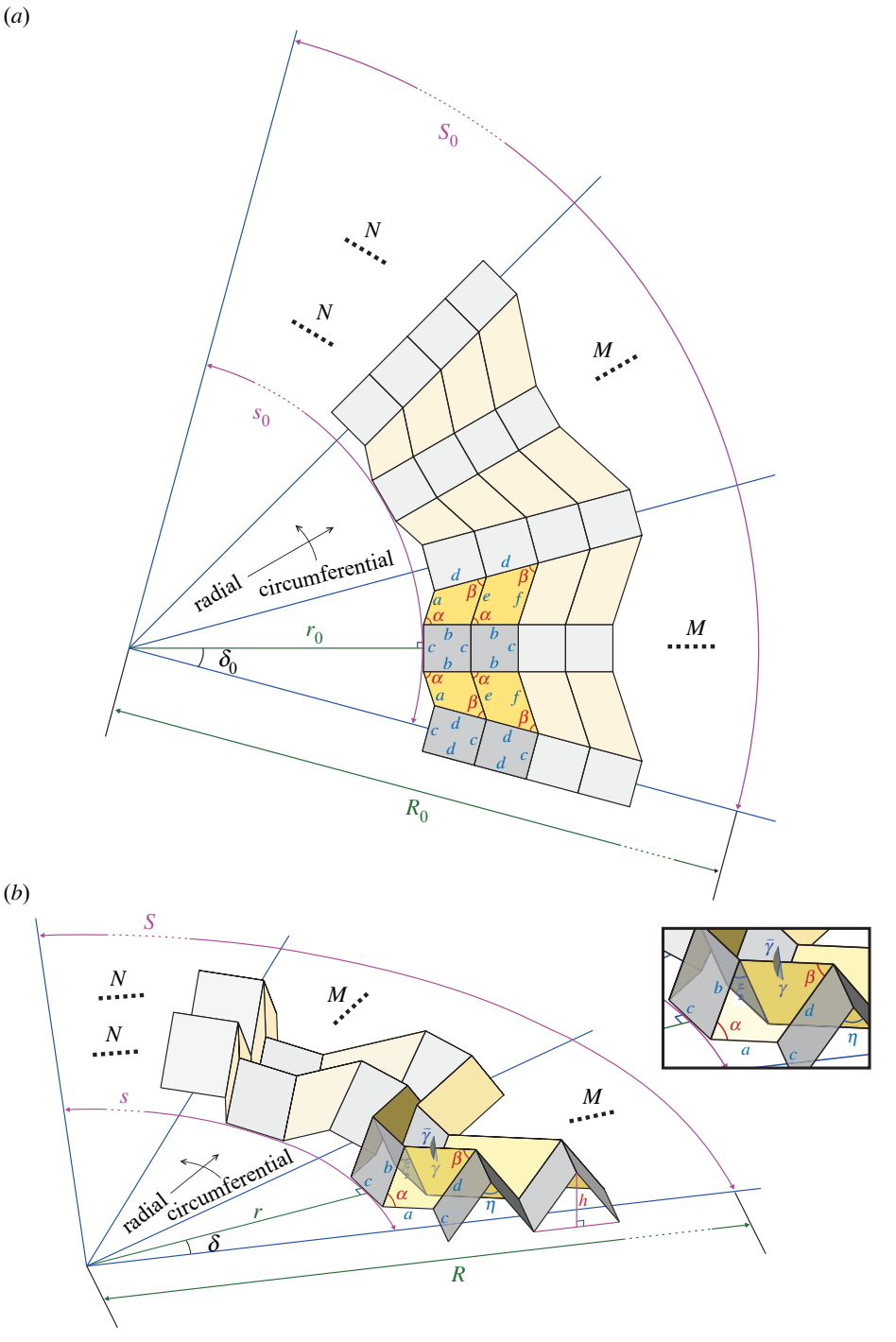

Figure 2. The unit cell and the tessellation of axisymmetric blockfold origami. (*a*) The flat unit cell (in dark yellow and grey) in the tessellation (in light yellow and grey). (*b*) The folded unit cell in the three-dimensional configuration of the tessellation.

and d. Two of the trapezoids are smaller with bases a and e, while the other two are larger with bases e and f. The edges of the trapezoids meet the following relationships

$$d = b\frac{\sin\alpha}{\sin\beta},\quad e = a + b\frac{\sin(\alpha-\beta)}{\sin\beta}\quad\text{and}\quad f = a + 2b\frac{\sin(\alpha-\beta)}{\sin\beta}. \tag{2.1}$$

Table 1. Geometric conditions of the Miura origami and its variants

type of origami	conditions
Miura origami	$0 < \alpha = \beta < \pi/2$ and $c = 0$
blockfold origami	$0 < \alpha = \beta < \pi/2$ and $c > 0$
axisymmetric Miura origami (AMO)	$0 < \alpha < \beta < \pi/2$ and $c = 0$
axisymmetric blockfold origami (ABO)	$0 < \alpha < \beta < \pi/2$ and $c > 0$

For the rectangles, two of them have side lengths b and c, while the other two have side lengths c and d. To build the whole origami pattern, firstly, the unit cell is replicated and rotated by $2\delta_0$ in the circumferential direction. Secondly, in the radial direction, the unit cell is replicated and translated by $2b$ while the trapezoid bases increased by $(f - a)$. The above procedures are repeated for M times in the radial direction and N times in the circumferential direction to generate an M-by-N ABO pattern. Altogether, the ABO pattern can be determined by the following parameters: the angles α and β, the side lengths a, b and c, and the repetitive numbers M and N. The overall radial size of the flat ABO pattern can be described by the inner radius r_0 and the outer radius R_0, as shown in figure 2*a*. We denote the included angle between the adjacent inner radius and outer radius by δ_0, which satisfies

$$\delta_0 = \alpha - \beta. \tag{2.2}$$

The inner radius r_0 and the outer radius R_0 can be calculated by

$$r_0 = c \times \frac{\cos\delta_0 + 1}{2\sin\delta_0} + a \times \frac{\sin\beta}{\sin\delta_0} \tag{2.3}$$

and

$$R_0 = c \times \frac{\cos\delta_0 + 1}{2\sin\delta_0} + a \times \frac{\sin\alpha}{\sin\delta_0} + 2Mb \times \frac{\sin\alpha}{\sin\beta}. \tag{2.4}$$

The detailed derivations for equations (2.3) and (2.4) are given in appendix A. For an M-by-N ABO pattern, we denote the total central angle by $\tilde{\delta}_0$, expressed as

$$\tilde{\delta}_0 = 2N\delta_0. \tag{2.5}$$

For the ABO crease pattern illustrated in figure 1*d*, we have $\tilde{\delta}_0 = 2\pi$. In addition, we define the inner perimeter

$$s_0 = \tilde{\delta}_0 r_0, \tag{2.6}$$

and the outer perimeter

$$S_0 = \tilde{\delta}_0 R_0. \tag{2.7}$$

The perimeters s_0 and S_0 describe the overall circumferential size of the ABO pattern.

The ABO pattern is general in the sense that we can degenerate the ABO pattern to the Miura pattern, the blockfold pattern and the AMO pattern, by changing the angles α and β, and the side length c. For a non-degenerate ABO pattern, the parameters should satisfy $0 < \alpha < \beta < \pi/2$ and $c > 0$. Without loss of generality, we have assumed $\alpha > \beta$, because interchanging the values of α and β only reverses the orientation of the origami pattern. The geometric conditions for the ABO and other three types of degenerate origami are summarized in table 1. If $\alpha = \beta$, the inner radius r_0 and the outer radius R_0 extend to infinity, and their included angle δ_0 decreases to zero. Consequently, the origami patterns lose their rotational symmetry and exhibit translational symmetry instead, corresponding to the Miura origami and the blockfold origami. If $c = 0$, the size of rectangles becomes zero, reminiscent of the Miura origami and the AMO, both of which are flat foldable.

(b) Three-dimensional geometry and non-flat-foldability

Now we switch to the three-dimensional configuration of ABO. As shown in figure 2*b*, by folding the unit cell and replicating it in the radial and circumferential directions, we can obtain the three-dimensional configuration of ABO. In figure 2*b*, we illustrate three representative dihedral angles γ, ξ and η. The angle γ is between the two trapezoids intersected at the edge e. The angle ξ is between the rectangles with sides b and c. The angle η is between the rectangles with sides c and d. The three dihedral angles describe the degree of folding of the three-dimensional ABO configuration, but are not independent variables. Specifically, the dihedral angles ξ and η can be determined by the dihedral angle γ as follows:

$$\boxed{\xi = \arccos(\sin^2\alpha\cos\gamma - \cos^2\alpha)} \tag{2.8}$$

and

$$\boxed{\eta = \arccos(\sin^2\beta\cos\gamma - \cos^2\beta).} \tag{2.9}$$

The detailed derivations for equations (2.8) and (2.9) are given in appendix A. The dihedral angle γ varies in the range $[0, \pi]$. The upper limit $\gamma = \pi$ corresponds to the unfolded and flat state of the origami, and the lower limit $\gamma = 0$ represents the fully folded state. Equation (2.8) indicates the one-to-one correspondence and monotonic dependence between the dihedral angles ξ and γ. Thus, substituting $\gamma = 0$ into equation (2.8) yields the minimum value for the dihedral angle ξ, denoted by $\xi_{\min} = \pi - 2\alpha$. Considering the basic condition $0 < \alpha < \pi/2$ for non-degenerate ABO patterns, we have $\xi_{\min} > 0$. Similarly, we can investigate equation (2.9) and obtain the non-zero minimum value for the dihedral angle η, denoted by $\eta_{\min} = \pi - 2\beta > 0$. Therefore, the dihedral angles ξ and η cannot be zero, indicating that ABO are non-flat-foldable.

We can also describe the non-flat-foldability of ABO by its overall volume V. To express the volume, we need to know the sizes of the three-dimensional configurations in the radial, circumferential and vertical directions. We use the inner radius r and the outer radius R to describe the overall radial size of the origami, as shown in figure 2*b*. The inner radius r and the outer radius R can be calculated by

$$r = c \times \frac{F(\alpha,\beta,\gamma)}{2\sin(\gamma/2)(\tan\alpha - \tan\beta)} + a \times \frac{G(\alpha,\gamma)}{\tan\alpha\cot\beta - 1} \tag{2.10}$$

and

$$R = c \times \frac{F(\alpha,\beta,\gamma)}{2\sin(\gamma/2)(\tan\alpha - \tan\beta)} + a \times \frac{G(\beta,\gamma)}{1 - \cot\alpha\tan\beta} + 2Mb \times \frac{G(\beta,\gamma)}{\csc\alpha\tan\beta}, \tag{2.11}$$

in which the functions $F(\alpha,\beta,\gamma)$ and $G(x,\gamma)$ are defined by

$$\left.\begin{aligned} F(\alpha,\beta,\gamma) &= 1 + \sin^2\left(\frac{\gamma}{2}\right)\tan\alpha\tan\beta + G(\alpha,\gamma)G(\beta,\gamma) \\ \text{and} \quad G(x,\gamma) &= \sqrt{1 + \sin^2\left(\frac{\gamma}{2}\right)\tan^2 x}. \end{aligned}\right\} \tag{2.12}$$

The angle included between the adjacent inner radius and outer radius is expressed as

$$\boxed{\delta = \arctan\left[\frac{\sin(\gamma/2)(\tan\alpha - \tan\beta)}{1 + \sin^2(\gamma/2)\tan\alpha\tan\beta}\right].} \tag{2.13}$$

The height h of the three-dimensional ABO configuration is given by

$$h = b\sin\alpha\cos\left(\frac{\gamma}{2}\right). \tag{2.14}$$

The detailed derivations for equations (2.8)–(2.14) are given in appendix A. Equations (2.8)–(2.14) indicate that, once the flat pattern of an ABO (say, α, β, a, b and c) is given, the three-dimensional configuration can be uniquely determined by the dihedral angle γ. For an M-by-N

ABO, we denote the central angle by $\tilde{\delta}$, expressed as

$$\tilde{\delta} = 2N\delta. \tag{2.15}$$

For the folded configuration of ABO illustrated in figure 1*d*, we have $\tilde{\delta} = 2\pi$. Corresponding to the perimeters s_0 and S_0 for the flat pattern, we define the inner perimeter

$$s = \tilde{\delta} r = 2N\delta r \tag{2.16}$$

and the outer perimeter

$$S = \tilde{\delta} R = 2N\delta R. \tag{2.17}$$

The perimeters s and S represent the overall circumferential size of the three-dimensional ABO configuration with respect to the dihedral angle γ. Given the radial sizes R and r, the circumferential sizes S and s, and the height h, the overall volume of ABO is expressed by

$$V = \frac{1}{2}(SR - sr)h. \tag{2.18}$$

We substitute equations (2.10), (2.11), (2.16) and (2.17) into equation (2.18), and calculate the Taylor series of V about $\gamma = 0$, which corresponds to the fully folded state. Then we obtain

$$\boxed{V = 2Nc\left(a + \frac{2Mb\sin\alpha}{\tan\beta}\right) + O(\gamma).} \tag{2.19}$$

According to equation (2.19), we know that the overall volume of a three-dimensional ABO configuration has a finite value even if the dihedral angle γ approaches zero. This again indicates the non-flat-foldability of ABO. It is worth noting that the non-flat-foldability can be transformed to flat-foldability by reducing the side length of the rectangles c to zero. In this scenario, the ABO degenerates to AMO.

3. Folding kinematics, closability and self-locking mechanisms of axisymmetric blockfold origami

We are interested in the ABO that form closed-ring shapes. Figure 1*d* shows a special example which is closed at both the flat unfolded state and a folded state. Generally speaking, an ABO that can be closed should satisfy the condition $\tilde{\delta}_{\max} \geq 2\pi$, in which $\tilde{\delta}_{\max}$ is the maximum central angle during the whole folding process of the origami. To obtain the expression of $\tilde{\delta}_{\max}$, we need to investigate the folding kinematics of ABO. We define a kinematic parameter

$$\tilde{\gamma} = \pi - \gamma. \tag{3.1}$$

The parameter $\tilde{\gamma}$ can be referred to as the folding angle that determines the three-dimensional configuration of ABO folded from its flat pattern. Substituting equations (3.1) and (2.13) into equation (2.15), we can rewrite $\tilde{\delta}$ as

$$\tilde{\delta}(\tilde{\gamma}) = 2N \arctan\left[\frac{\cos(\tilde{\gamma}/2)(\tan\alpha - \tan\beta)}{1 + \cos^2(\tilde{\gamma}/2)\tan\alpha\tan\beta}\right], \tag{3.2}$$

in which $\tilde{\gamma} \in [0, \pi]$. Specifically, $\tilde{\gamma} = 0$ represents the flat unfolded state, and $\tilde{\gamma} = \pi$ represents the fully folded state. To derive the expression of $\tilde{\delta}_{\max}$, first, we take the derivative of $\tilde{\delta}(\tilde{\gamma})$ with respect to $\tilde{\gamma}$:

$$\tilde{\delta}'(\tilde{\gamma}) = \frac{\mathrm{d}\tilde{\delta}}{\mathrm{d}\tilde{\gamma}} = \frac{N\sin(\tilde{\gamma}/2)(\tan\alpha - \tan\beta)}{[G(\alpha,\gamma)G(\pi-\beta,\gamma)]^2}[\cos^2(\tilde{\gamma}/2)\tan\alpha\tan\beta - 1], \tag{3.3}$$

in which the function $G(x, \gamma)$ is given in equation (2.12). If $0 < \alpha + \beta \leq \pi/2$, the inequality $\tan\alpha\tan\beta \leq 1$ holds true. In addition, we recall that for all the ABO, the angles α and β meet the precondition $0 < \beta < \alpha < \pi/2$, which implies $\tan\alpha > \tan\beta$. Then we have $\tilde{\delta}'(\tilde{\gamma}) < 0$ over $(0, \pi]$ and

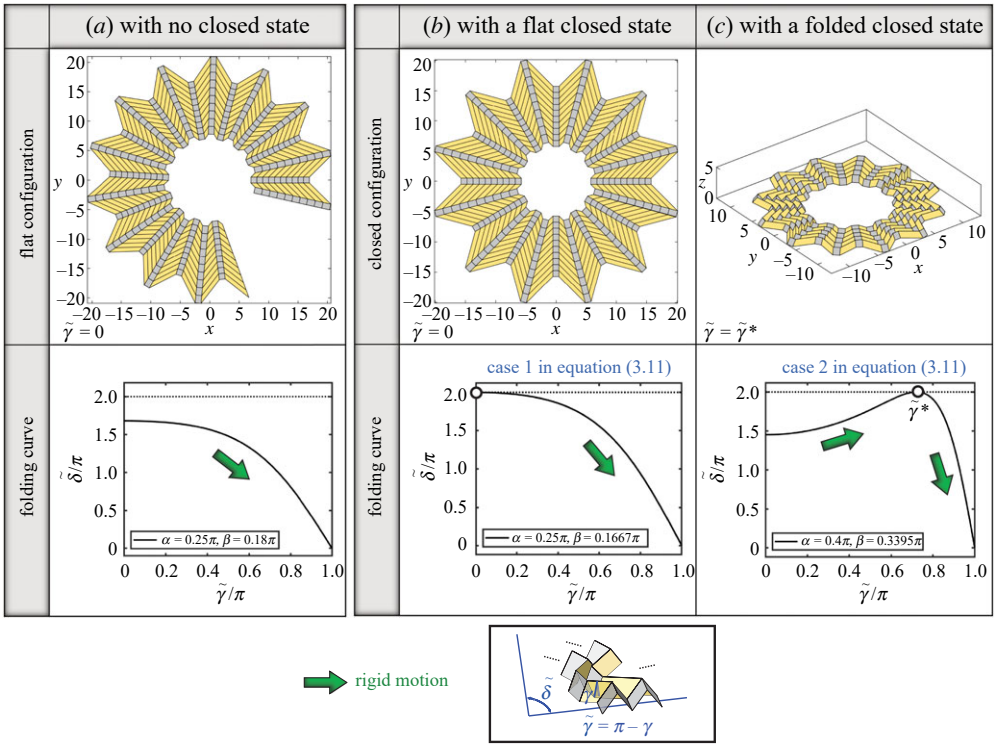

Figure 3. The folding kinematics of axisymmetric blockfold origami without self-locking mechanisms for different closability: (*a*) with no closed state, (*b*) with a flat closed state and (*c*) with a closed-folded state.

$\tilde{\delta}'(0) = 0$. Otherwise if $\pi/2 < \alpha + \beta < \pi$, the inequality $\tan\alpha \tan\beta > 1$ holds true. Then we have $\tilde{\delta}'(\tilde{\gamma}) > 0$ over $(0, \gamma^\star)$, $\tilde{\delta}'(\tilde{\gamma}^\star) = 0$, and $\tilde{\delta}'(\tilde{\gamma}) < 0$ over $(\gamma^\star, \pi]$, in which

$$\tilde{\gamma}^\star = 2\arccos\left(\frac{1}{\sqrt{\tan\alpha \tan\beta}}\right). \tag{3.4}$$

Altogether, the variation of the central angle $\tilde{\delta}$ with the folding angle $\tilde{\gamma}$ can be divided into the following two situations:

— If $0 < \alpha + \beta \le \pi/2$, $\tilde{\delta}(\tilde{\gamma})$ is decreasing over $[0, \pi]$.
— If $\pi/2 < \alpha + \beta < \pi$, $\tilde{\delta}(\tilde{\gamma})$ is increasing over $[0, \tilde{\gamma}^\star]$ and is decreasing over $(\tilde{\gamma}^\star, \pi]$.

By substituting $\tilde{\gamma} = 0$ and $\tilde{\gamma}^\star$ into $\tilde{\delta}(\tilde{\gamma})$, we obtain the expression of $\tilde{\delta}_{\max}$ as

$$\tilde{\delta}_{\max} = \begin{cases} 2N(\alpha - \beta), & \text{if } 0 < \alpha + \beta \le \dfrac{\pi}{2}, \\ 2N \arctan[H(\alpha, \beta)], & \text{if } \dfrac{\pi}{2} < \alpha + \beta < \pi, \end{cases} \tag{3.5}$$

in which the function $H(\alpha, \beta)$ is defined by

$$H(\alpha, \beta) = \frac{\tan\alpha - \tan\beta}{2\sqrt{\tan\alpha \tan\beta}}. \tag{3.6}$$

Obviously, if $\tilde{\delta}(\tilde{\gamma})$ is monotonically decreasing and the flat pattern is not closed, the ABO cannot form closed-ring shapes throughout the folding process. Figure 3*a* gives an example of ABO with no closed state. The angles $\alpha = 0.25\pi$ and $\beta = 0.18\pi$ and the circumferential unit cell number $N = 12$ satisfy $0 < \alpha + \beta \le \pi/2$ and $2N(\alpha - \beta) < 2\pi$. While the central angle $\tilde{\delta}(\tilde{\gamma})$ is in non-monotonic

variation, the unclosability condition reads $\pi/2 < \alpha + \beta < \pi$ and $2N \arctan[H(\alpha, \beta)] < 2\pi$, which means at the extreme point $\tilde{\gamma}^\star$, the maximum central angle $\tilde{\delta}_{\max}$ is less than 2π.

When the maximum central angle $\tilde{\delta}_{\max} \geq 2\pi$, the ABO can have at least one closed configuration. Now we derive the expression of the folding angle $\tilde{\gamma}$ corresponding to the closed configurations. Considering equation (3.5) with the basic relationships $\alpha - \beta < \pi/2$ for non-degenerate ABO and $\arctan[H(\alpha, \beta)] < \pi/2$ for the inverse tangent function, we know that $\tilde{\delta}_{\max} < N\pi$. Therefore, to guarantee that $\tilde{\delta}_{\max} \geq 2\pi$, the circumferential unit cell number N should satisfy

$$N \geq 3, \tag{3.7}$$

which is necessary for any closed configuration of ABO. For the convenience of the following formulations, we define two functions $L(\alpha, \beta)$ and $T(N)$

$$L(\alpha, \beta) = \sqrt{\frac{\tan\alpha}{\tan\beta}} \quad \text{and} \quad T(N) = \tan\left(\frac{\pi}{4} + \frac{\pi}{2N}\right). \tag{3.8}$$

Then we can rewrite $H(\alpha, \beta)$ as

$$H(\alpha, \beta) = \frac{1}{2}\left[L(\alpha, \beta) - \frac{1}{L(\alpha, \beta)}\right], \tag{3.9}$$

and we have the following equivalence:

$$\tilde{\delta}_{\max} \geq 2\pi \Leftrightarrow \begin{cases} \alpha - \beta \geq \dfrac{\pi}{N}, & \text{if } 0 < \alpha + \beta \leq \dfrac{\pi}{2}, \\ L(\alpha, \beta) \geq T(N), & \text{if } \dfrac{\pi}{2} < \alpha + \beta < \pi. \end{cases} \tag{3.10}$$

The condition (3.10) guarantees the ABO can form closed-ring shapes. Under this condition, we solve the equation $\tilde{\delta}(\tilde{\gamma})|_{\tilde{\gamma}=\tilde{\gamma}_c} = 2\pi$ and obtain

$$\tilde{\gamma}_c = \begin{cases} 0, & (\text{case 1) if } 0 < \alpha + \beta \leq \dfrac{\pi}{2} \text{ and } \alpha - \beta = \dfrac{\pi}{N}, \\ \tilde{\gamma}^\star, & (\text{case 2) if } \dfrac{\pi}{2} < \alpha + \beta < \pi \text{ and } \alpha - \beta < \dfrac{\pi}{N} \text{ and } L(\alpha, \beta) = T(N), \\ \tilde{\gamma}_+ \text{ or } \tilde{\gamma}_-, & (\text{case 3) if } \dfrac{\pi}{2} < \alpha + \beta < \pi \text{ and } \alpha - \beta < \dfrac{\pi}{N} \text{ and } L(\alpha, \beta) > T(N), \\ 0 \text{ or } \tilde{\gamma}_-, & (\text{case 4) if } \dfrac{\pi}{2} < \alpha + \beta < \pi \text{ and } \alpha - \beta = \dfrac{\pi}{N}, \\ \tilde{\gamma}_-, & (\text{case 5) if } \alpha - \beta > \dfrac{\pi}{N}, \end{cases} \tag{3.11}$$

in which $\tilde{\gamma}_\pm$ is given by

$$\tilde{\gamma}_\pm = 2\arccos\left[\frac{H(\alpha, \beta) \pm \sqrt{[H(\alpha, \beta)]^2 - \tan^2(\pi/N)}}{\sqrt{\tan\alpha \tan\beta}\tan(\pi/N)}\right]. \tag{3.12}$$

The solutions $\tilde{\gamma}_c$ are the folding angles at which the ABO form closed-ring shapes. The detailed derivation of equations (3.10)–(3.12) is given in appendix B. Equation (3.11) divides the expression of $\tilde{\gamma}_c$ into five cases, in which we have $0 < \tilde{\gamma}_+ < \tilde{\gamma}_-$ for the third case and $\tilde{\gamma}_- > 0$ for the fourth case and the fifth case. The five cases correspond to different folding behaviours of ABO while all of them have closed configurations. In the first case, the ABO are closed at the initial flat state and the central angle decreases monotonically upon folding. Figure 3*b* gives an example of ABO with a flat closed configuration. The angles $\alpha = 0.25\pi$ and $\beta = 0.1667\pi$ and the circumferential unit cell number $N = 12$ satisfy $0 < \alpha + \beta \leq \pi/2$ and $\alpha - \beta = \pi/N$.

In the second case, the central angle $\tilde{\gamma}$ varies non-monotonically, and the ABO form the closed configuration at the extreme folding angle $\tilde{\gamma}^\star$. Figure 3*c* gives an example of ABO with a closed-folded configuration. The angles $\alpha = 0.4\pi$ and $\beta = 0.3395\pi$ and the circumferential unit cell number $N = 12$ satisfy $\pi/2 < \alpha + \beta < \pi$ and $\alpha - \beta < \pi/N$ and $L(\alpha, \beta) = T(N)$.

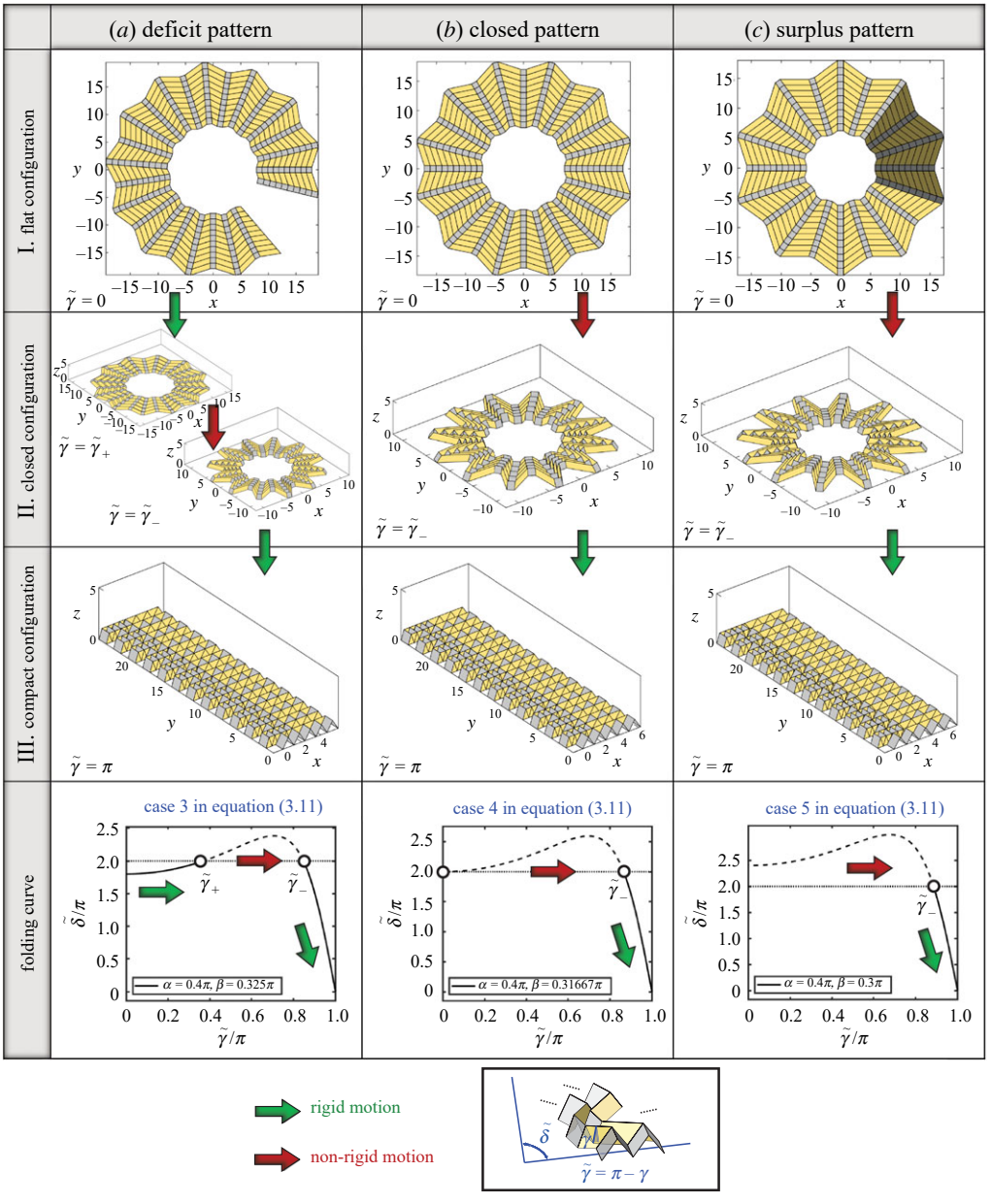

Figure 4. The folding kinematics of axisymmetric blockfold origami with self-locking mechanisms for different flat patterns: (*a*) deficit pattern, (*b*) closed pattern and (*c*) surplus pattern.

The ABO in both the first and the second cases can be folded in continuous rigid motion from the flat state to the fully folded state. By contrast, in the third case, the central angle of the flat pattern is less than 2π, and in theory, the non-monotonic folding motion allows the central angle to increase to larger than 2π. As a result, the ABO has two closed-folded configurations corresponding to $\tilde{\gamma}_{\pm}$. However, the configurations between $\tilde{\gamma}_{+}$ and $\tilde{\gamma}_{-}$ are invalid in physics because the rigid panels cannot intersect with each other to make the central angle exceed 2π. In other words, there exists a region between the flat state and the fully folded state that the ABO cannot reach through rigid folding. Figure 4*a* gives an example of ABO with two closed-folded configurations. The angles $\alpha = 0.4\pi$ and $\beta = 0.325\pi$ and the circumferential unit cell number

$N = 12$ satisfy $\pi/2 < \alpha + \beta < \pi$ and $\alpha - \beta < \pi/N$ and $L(\alpha, \beta) > T(N)$. If the panels are rigid, the ABO gets self-locked when folded to the closed state at $\tilde{\gamma} = \tilde{\gamma}_+$. The folding cannot proceed unless the panels deform to cross the barrier between $\tilde{\gamma}_+$ and $\tilde{\gamma}_-$, which results in non-rigid motion. Once the ABO arrives at the other closed state at $\tilde{\gamma} = \tilde{\gamma}_-$, the folding can continue in rigid motion and finally stops at the fully folded compact state. Because of the non-flat-foldability, the ABO occupies a finite volume at the compact state with the blocked configuration, which are different from the flat-foldable Miura origami or AMO. The flat pattern of the ABO in the third case has a central angle less than 2π, which we call a deficit pattern. In this case, the non-monotonic variation of the central angle plays a fundamental role in the self-locking mechanisms. Otherwise if the central angle varies monotonically, no self-locking phenomenon will emerge as shown in the previous example in figure 3*a*.

The self-locking mechanisms do not necessitate a deficit pattern. In the fourth case, the ABO have closed flat patterns, and the non-monotonic variation of the central angle induces a closed-folded configuration. Figure 4*b* gives an example of ABO with a closed flat pattern and a closed-folded configuration. The angles $\alpha = 0.4\pi$ and $\beta = 0.31667\pi$ and the circumferential unit cell number $N = 12$ satisfy $\pi/2 < \alpha + \beta < \pi$ and $\alpha - \beta = \pi/N$. Again, the transition between the two closed states can only be achieved through non-rigid folding. In this case, the self-locking in rigid folding motion happens at the initial flat state, which is also dominated by the non-monotonic variation of the central angle.

However, if the flat pattern is surplus, which means the initial central angle $\tilde{\delta}(0)$ is greater than 2π, the self-locking mechanism always exists whether the variation of the central angle is monotonic or not. This is the fifth case, in which the ABO have surplus flat patterns and no other constraints on the monotonicity are applied. Figure 4*c* gives an example of ABO with a surplus flat pattern and a closed-folded configuration. The angles $\alpha = 0.4\pi$ and $\beta = 0.3\pi$ and the circumferential unit cell number $N = 12$ satisfy $\alpha - \beta > \pi$. The surplus pattern has an overlapping area with two layers of panels. If the panels are rigid, the ABO cannot be folded to the three-dimensional closed state, and therefore is self-locked at the initial flat state. Finally, we remark that, for the ABO represented by three examples shown in figure 4, the self-locking mechanisms can also be observed and described in terms of the deployment process, that is, with the kinematic parameter $\tilde{\gamma}$ varying from π to 0. In this way, the ABO in figure 4 are self-locked at $\tilde{\gamma} = \tilde{\gamma}_-$ when deployed from the fully folded and blocked configurations.

For more visual details, we refer to the supplemental Movie 1 for the animations of the folding kinematics of all the ABO illustrated in figures 3 and 4.

From the above analysis, we know that the values of the angles α and β and the circumferential unit cell number N determine the folding kinematics of ABO. To visualize this, in figure 5, we demonstrate contour plots of the maximum central angle $\tilde{\delta}_{\max}$ with the angles α and β for different circumferential unit cell number N. Figure 5*a* shows the contour plot for $N = 12$ with scatters accommodating the examples of ABO given in figures 3 and 4. The whole feasible domain of (α, β) is the triangular region confined by the condition $0 < \alpha < \beta < \pi/2$, which is applied to all ABO as summarized in table 1. The triangular region is divided into two parts demarcated by the red solid line $\alpha - \beta = \pi/N$ for $\alpha + \beta \leq \pi/2$ and the yellow solid line $L(\alpha, \beta) = T(N)$ for $\alpha + \beta > \pi/2$. The lines of demarcation and the region below them are described by the condition (3.10), and therefore correspond to the ABO that have closed configurations. By contrast, the region above the lines of demarcation corresponds to the ABO that cannot form closed-ring shapes. The red solid line of demarcation represents the ABO that have a closed flat pattern with monotonic folding kinematics, as shown in figure 3*b*. The yellow solid line of demarcation represents the ABO that have a deficit flat pattern and a closed-folded configuration induced by the non-monotonic folding kinematics, as shown in figure 3*c*. The red dashed line is the extension of the red solid line into the non-monotonic-folding region for $\alpha + \beta > \pi/2$, and thus represents the ABO that have a closed flat pattern and a closed-folded configuration, as shown in figure 4*b*. As such, the solid lines of demarcation and the region below them correspond to the ABO that have self-locking mechanisms. Above the solid lines is the non-locking region where the ABO can be folded in continuous rigid motion from the flat state to the fully folded blocked state. Figure 5*b*,*c* shows the

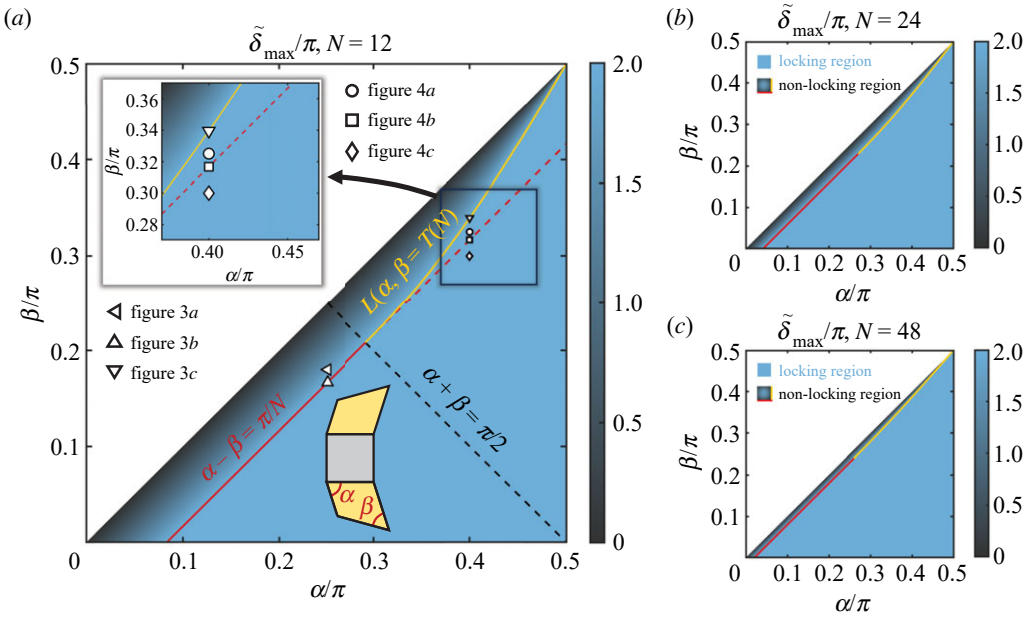

Figure 5. Contour plot of the maximum central angle $\tilde{\delta}_{max}$ with the angles α and β for different circumferential number of unit cells N: (*a*) $N = 12$, (*b*) $N = 24$ and (*c*) $N = 48$. Note that as the number of unit cells increases, the locking region shrinks.

contour plots for $N = 24$ and $N = 48$, respectively. We can see that the non-locking region shrinks with the increase of the circumferential unit cell number N. This indicates that the closability and the self-locking mechanisms are destined to arise if the number of the circumferential unit cells is large enough.

To end this section, we remark that the formulations of the geometry of ABO can be directly applied to AMO by setting $c = 0$. The kinematics of ABO depends only on the angles α and β and the circumferential unit cell number N, and independent from side lengths a, b and c. Therefore, the formulations of the kinematics of ABO in the current paper are consistent with the deployment analysis of AMO in [25]. The kinematics analysis in the current paper aims to give more concise formulations and to provide more insights into the self-locking mechanisms and closability of the family of axisymmetric Miura variants including both ABO and AMO.

4. Enhanced stiffness of axisymmetric blockfold origami

Inspired from blockfold origami, we are interested to explore the mechanical properties of ABO. To this end, we used the origami structural analysis software MERLIN [30,31] to perform quasi-static compression test simulations on the ABO with different sizes of rectangular panels. The ABO structures in our simulations are shown in figure 6*a*. The geometric and kinematic parameters that determine the ABO structures are given in table 2. The only difference in the four origami structures is the edge length c of the rectangular panels. Specially, when $c = 0$, the ABO degenerates to AMO. We selected the interior angles $\alpha = 0.4\pi$ and $\beta = 0.275\pi$ and circumferential unit cell number $N = 8$, which belong to case 4 in equation (3.11). In this case, we set the folding angle $\tilde{\gamma} = \tilde{\gamma}_{-} = 0.821\pi$ corresponding to the closed-folded configurations of the ABO. The ABO in case 4 have a closed flat pattern and a closed-folded configuration (figure 4*b*). This characteristic benefits the practical manufacture of closed-folded ABO structures, especially as candidates for foldcores of sandwich composites. The reason is that one can directly fold a closed flat sheet through non-rigid motion to get the three-dimensional closed axisymmetric structure, which is easier compared to folding a sheet with a cut through the radius and then gluing the gap. If the

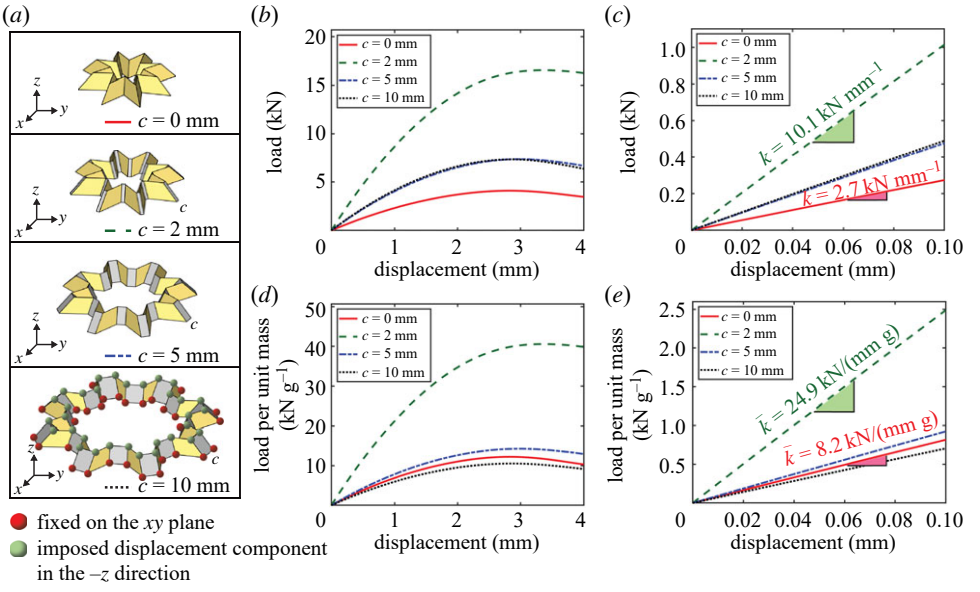

Figure 6. Load–displacement curves of the quasi-static compression test simulations of the axisymmetric blockfold origami for different sizes of rectangular panels. (*a*) The axisymmetric blockfold origami configurations for the compression test simulations. The first axisymmetric blockfold origami degenerates to axisymmetric Miura origami with $c = 0$. For each origami, the bottom vertices are fixed on the *xy* plane; the top vertices are controlled by their displacements in the minus *z* direction with free movements in the *x* and *y* directions. (*b*) The absolute load versus large displacement. (*c*) The absolute load versus the small displacement. (*d*) The load per unit mass versus the large displacement. (*e*) The load per unit mass versus the small displacement.

Table 2. Geometric and kinematic parameters of the ABO for compression test simulations.

geometric and kinematic parameters	value(s)
side length *a*	6 mm
side length *b*	10 mm
side length *c*	0, 2 mm, 5 mm, 10 mm
interior angle α	0.4π
interior angle β	0.275π
folding angle $\tilde{\gamma}$	0.821π
radial unit cell number *M*	1
circumferential unit cell number *N*	8

flat sheet is real paper or plastic film, the creases can be perforated by light-duty cutting machines or laser cutting systems, and the folding can be done by hand [32]. If the flat sheet is made of metal, the creases can be perforated by CNC milling machines and the folding can be done through the cold gas-pressure process [33] or punch stamping process [20].

The material properties and other MERLIN settings for our compression test simulations are listed in table 3. We set the material properties as typical values of real paper: 'ModElastic' (elastic modulus) 1000 MPa, 'Poisson' (Poisson's ratio) 0.3, 'Thickness' (thickness) 0.1 mm and the ratio of length-scale factor 'LScaleFactor' 2, which determines the rotational modulus of the creases. Detailed definition and typical values of 'LScaleFactor' can be found in [34]. We used the 'N5B8' bar-and-hinge model (ModelType) to capture realistic doubly curved out-of-plane deformations and isotropic in-plane behaviours of the origami panels. The material calibration method (MaterCalib) was set as 'auto' to specify the constitutive models implicitly

Table 3. Material properties and simulation options assigned to the compression test simulations in MERLIN.

material properties	value
ModElastic	1000 MPa
Poisson	0.3
thickness	0.1 mm
simulation options	**value**
ModelType	N5B8
MaterCalib	auto
LScaleFactor	2
LoadType	displacement
DispStep	200

based on the input material properties using the formulae defined in [34]. For each origami in figure 6*a*, the bottom vertices were fixed on the xy plane; the top vertices were controlled by their displacements (LoadType) in the minus z direction with free movements in the x and y directions. The displacements were applied in 200 incremental steps (DispStep) from 0 to 4 mm, which are approximately half of the height of the origami $h = 9.14$ mm. The height h can be calculated from equations (2.14) and (3.1) with the parameters given in table 2. Figure 6*b* illustrates the load–displacement curves of the compression test simulations for the four origami. We can see that the applied displacements were large enough to induce deformation of the origami, which changes from compression dominated by the bars to folding/bending dominated by the hinges in the computational simulation. By adding slender rectangular panels to build the ABO ($c = 2$ mm) from the AMO ($c = 0$), we dramatically increased the peak load by about four times from 4.1 kN to 16.6 kN. However, larger rectangular panels (say, $c = 5$ mm and 10 mm) cannot further increase the peak load. Instead, the peak loads drop back to around 7.3 kN for both the ABO with $c = 5$ mm and 10 mm. This may be related to the fact that the critical stress of rectangular plate buckling is inversely proportional to the square of the width of the plate [35]. To compare the stiffness of the origami in their linear deformation regions, we extracted the initial parts of the load–displacement curves with the displacement varying from 0 to 0.1 mm, as shown in figure 6*c*. We can see that the ABO with $c = 2$ mm has the linear stiffness 10.1 kN/(mm · g), which is more than three times as high as the 2.7 kN mm^{-1} of the AMO with $c = 0$. Importantly, the mass of the rectangular panels with $c = 2$ mm is very small compared to the whole origami structure. To visualize this point, we divided the load by the mass of the origami structures and reproduced the load–displacement curves, as illustrated in figure 6*d* for the large deformations and in figure 6*e* for the small deformations. We calculated the mass of the panels by using the parameters in table 2 and the typical density of paper 0.001 g mm^{-3}. In figure 6*d*, we can see that the peak load per unit mass of the ABO with $c = 2$ mm is about 40.6 kN g^{-1}, which is still nearly four times as high as the 12.2 kN g^{-1} of the AMO with $c = 0$. However, when we further increased the size of the rectangular panels, the increase of mass and the increase of the peak load cancelled out, and as a result, the peak loads per unit mass of the ABO with $c = 5$ mm and 10 mm are approximately at the same level as the AMO. Similarly, in figure 6*e*, the ABO with $c = 2$ mm has the linear stiffness per unit mass 24.9 kN/(mm · g), which is still about three times as high as the 8.2 kN/(mm · g) of the AMO with $c = 0$. By contrast, the linear stiffness per unit mass of the ABO with $c = 5$ mm and 10 mm has no significant difference to that of the AMO.

To further compare the load-bearing capacity of the ABO and AMO, in figure 7, we show the variations of the loads at different nodes of the origami structures. Figure 7*a* shows the load–displacement curve of the whole structure and node A and node B of the ABO with $c = 0.2$ mm. Node A and node B belong to the same trapezoid panel. We can see that node B bears more load than node A does. Figure 7*b* shows the load–displacement curve of the whole structure and node

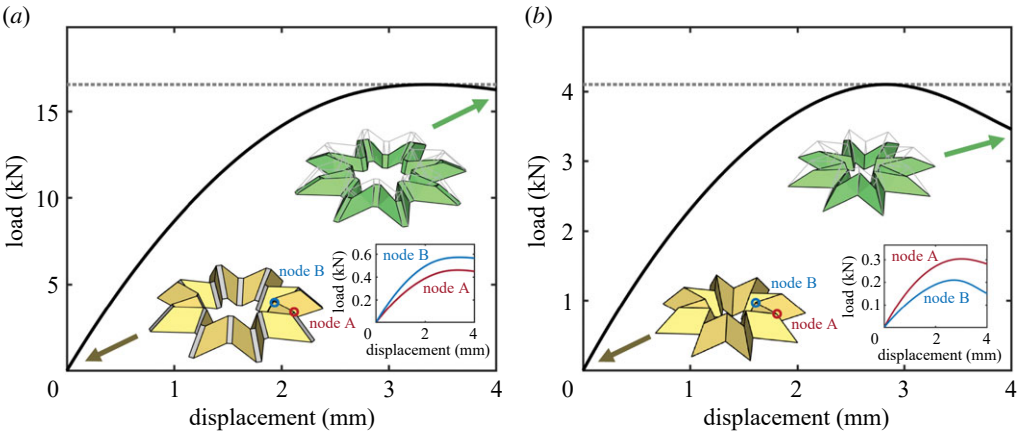

Figure 7. Load–displacement curves of the compression test simulations of (*a*) the axisymmetric blockfold origami and (*b*) the axisymmetric Miura origami.

A and node B of the AMO with $c = 0$. Again, node A and node B belong to the same trapezoid panel. We can see that node A bears more load than node B does, and this gap expands quickly after the origami reaches the peak load. The discrepancy between the load distributions of AMO and ABO is induced by the existence of the rectangular panels in the latter pattern. Altogether, the enhanced stiffness and the increased load-bearing capacity of the ABO, especially of those with rectangular panels of relatively small sizes, suggest the promising potential applications of the ABO such as foldcores of sandwich composites.

5. Prospects for tightly stacked axisymmetric origami structures

We extend the contents of the paper by demonstrating a tightly stacked axisymmetric origami structure. The stacked origami structure is composed of alternative layers of ABO and AMO, as shown in figure 8*a*. The ABO was generated by the angles $\alpha = 0.4\pi$, $\beta = 0.275\pi$ and $\tilde{\gamma} = 0.821\pi$; the side lengths $a = 9$ mm, $b = 15$ mm and $c = 9$ mm; and the cell numbers $M = 3$ and $N = 8$. The AMO has the same geometric parameters as those of the ABO, except that the AMO has no rectangular panels (i.e. $c = 0$). The key point is that the three-dimensional configurations of the aforementioned AMO and ABO are not rigidly compatible, which means they can only be tightly stacked with deformations of their panels. Figure 8*b* illustrates the stacking strategy, by which we move the panels of the ABO to make them fit into the slots of the AMO, creating tight line contacts and point contacts between the AMO and the ABO. To make a physical model, we used a laser cutter (Universal Laser Systems) to cut the outlines and to engrave the creases on the paper (Canson, 150 GSM), as shown in figure 8*c*. Then we folded the paper along the creases and assembled them into a tight structure, as shown in figure 8*d*. We used transparent elastic bands to tie the structure up so as to confine its shape. Figure 8*e* illustrates the front view of the structure with four layers of ABO and three layers of AMO (invisible) between the ABO. The ABO and the AMO are stacked in tight contact because the mismatch of their rigid configurations induces prestress in the assembling process. The prestress is anticipated to contribute to the stability and load-bearing capacity, which is left for future work.

6. Concluding remarks

In summary, we propose a family of non-flat-foldable Miura-variant origami with rotational symmetry, which we name the ABO. We characterize the geometry of the flat patterns and the three-dimensional folded configurations of the ABO. We investigate the folding kinematics of the ABO and derive the conditions regarding the geometric parameters under which the ABO can

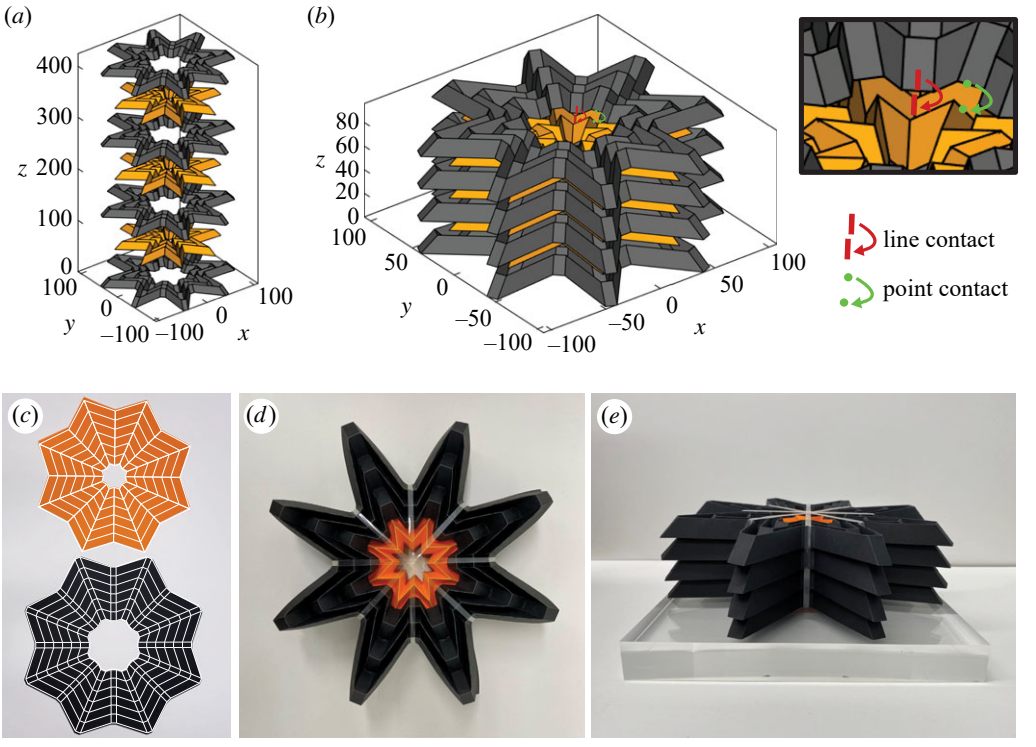

Figure 8. The stacked axisymmetric origami structure. (*a*) The axisymmetric blockfold origami and the axisymmetric Miura origami that are used to assemble the stacked origami structure. (*b*) The stacking strategy. The green and red arrows indicate the locations where the AMO and the ABO join each other. (*c*) The unfolded paper for the axisymmetric blockfold origami (in black colour) and the axisymmetric Miura origami (in orange colour). The white lines are added to highlight the creases. (*d*) The stacked origami structure with prestress (top view). (*e*) The stacked origami structure (front view). The transparent elastic bands are used to confine the shape of the origami structure.

exhibit the closed ring-shape three-dimensional configurations and the self-locking behaviours. We performed compression test simulations for the ABO with rectangular panels of different sizes. The simulation results indicate that by trading off a slight increase of mass from the rectangular panels, we can obtain a significant enhancement of the stiffness and dramatic increase of the load-bearing capacity of the ABO structures compared to the AMO. As an extension of the current work, we propose a stacking strategy for tightly stacked axisymmetric origami structures which takes advantage of the prestress induced by the mismatch of the ABO and AMO in successive layers.

Data accessibility. The data are provided in electronic supplementary material [36].

Declaration of AI use. We have not used AI-assisted technologies in creating this article.

Authors' contributions. X.D.: conceptualization, data curation, formal analysis, investigation, methodology, software, validation, visualization, writing—original draft, writing—review and editing; G.H.P.: conceptualization, funding acquisition, investigation, methodology, project administration, resources, software, supervision, writing—review and editing.

All authors gave final approval for publication and agreed to be held accountable for the work performed therein.

Conflict of interest declaration. We declare we have no competing interests.

Funding. The research was supported by the National Science Foundation (NSF) through grant No. 2323276.

Acknowledgements. The authors appreciate the helpful comments provided by Kevin T. Liu from Princeton University.

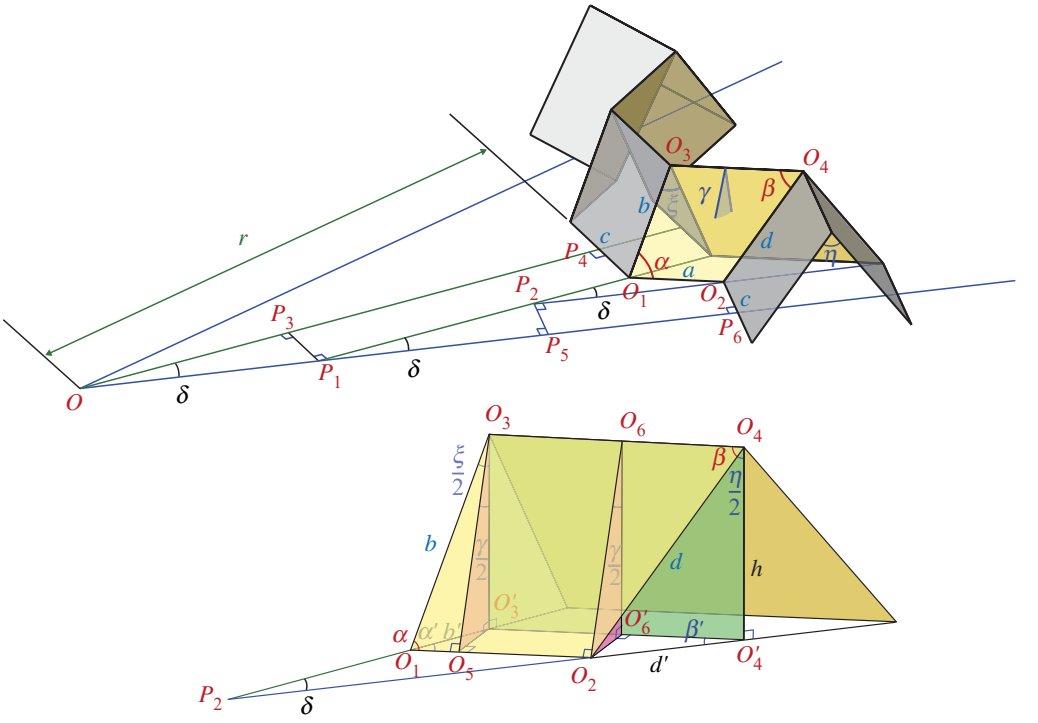

Figure 9. Notation for the geometric elements of the ABO unit cell.

Appendix A. Derivation of geometric relationships

Figure 9 illustrates supplemental notations of the three-dimensional unit cell in figure 2*b*. The notations include the points O, O_i, P_i, $i = 1, 2, \ldots, 6$, the points O'_3, O'_4 and O'_6, the angles α' and β', the sides b' and d', and the height h. The prime superscript indicates that the geometric element is vertically projected to the bottom plane of the origami. Specifically, O'_3, O'_4 and O'_6 are the projection points of O_3, O_4 and O_6, respectively; α' and β' are the projection angles of α and β, respectively; b' and d' are the projection sides of b and d, respectively. The projection angle α' satisfies

$$\tan\alpha' = \frac{|O'_3O_5|}{|O_1O_5|} = \frac{|O'_3O_5|}{|O_3O_5|}\frac{|O_3O_5|}{|O_1O_5|} = \sin\frac{\gamma}{2}\tan\alpha. \tag{A 1}$$

The dihedral angle ξ satisfies

$$\sin\frac{\xi}{2} = \frac{|O_1O'_3|}{|O_1O_3|} = \frac{|O_1O'_3|}{|O_1O_5|}\frac{|O_1O_5|}{|O_1O_3|} = \frac{\cos\alpha}{\cos\alpha'} \tag{A 2}$$

and

$$\cos\xi = 1 - 2\sin^2\left(\frac{\xi}{2}\right). \tag{A 3}$$

Combining equations (A 1)–(A 3), we can derive

$$\begin{aligned}\cos\xi &= 1 - \frac{2\cos^2\alpha}{\cos^2\alpha'}\\ &= 1 - 2\cos^2\alpha(1 + \tan^2\alpha')\\ &= 1 - 2\cos^2\alpha\left[1 + \sin^2\left(\frac{\gamma}{2}\right)\tan^2\alpha\right]\end{aligned}$$

$$= \sin^2\alpha\left[1-2\sin^2\left(\frac{\gamma}{2}\right)\right]-\cos^2\alpha$$
$$= \sin^2\alpha\cos\gamma-\cos^2\alpha. \tag{A 4}$$

Considering $\xi\in[0,\pi]$, we obtain the expression of ξ in equation (2.8). The expression of the dihedral angle η can be obtained by following the similar procedure. The angles β' and η satisfy

$$\tan\beta'=\frac{|O_2O_6'|}{|O_4'O_6'|}=\frac{|O_2O_6'|}{|O_2O_6|}\frac{|O_2O_6|}{|O_4O_6|}\frac{|O_4O_6|}{|O_4'O_6'|}=\sin\frac{\gamma}{2}\tan\beta, \tag{A 5}$$

$$\sin\frac{\eta}{2}=\frac{|O_2O_4'|}{|O_2O_4|}=\frac{|O_2O_4'|}{|O_4'O_6'|}\frac{|O_4'O_6'|}{|O_4O_6|}\frac{|O_4O_6|}{|O_2O_4|}=\frac{\cos\beta}{\cos\beta'} \tag{A 6}$$

and

$$\cos\eta=1-2\sin^2\left(\frac{\eta}{2}\right). \tag{A 7}$$

For the derivations in equations (A 5) and (A 6), we have applied $|O_4O_6|=|O_4'O_6'|$. Combining equations (A 5)–(A 7), we can derive

$$\cos\eta=1-\frac{2\cos^2\beta}{\cos^2\beta'}$$
$$=1-2\cos^2\beta(1+\tan^2\beta')$$
$$=1-2\cos^2\beta\left[1+\sin^2\left(\frac{\gamma}{2}\right)\tan^2\beta\right]$$
$$=\sin^2\beta\left[1-2\sin^2\left(\frac{\gamma}{2}\right)\right]-\cos^2\beta$$
$$=\sin^2\beta\cos\gamma-\cos^2\beta. \tag{A 8}$$

Considering $\eta\in[0,\pi]$, we obtain the expression of η in equation (2.9). The included angle δ can be simply given by

$$\delta=\alpha'-\beta'. \tag{A 9}$$

Then, we combine equations (A 1), (A 5) and (A 9) and derive

$$\tan\delta=\tan(\alpha'-\beta')$$
$$=\frac{\tan\alpha'-\tan\beta'}{1+\tan\alpha'\tan\beta'}$$
$$=\frac{\sin(\gamma/2)(\tan\alpha-\tan\beta)}{1+\sin^2(\gamma/2)\tan\alpha\tan\beta}. \tag{A 10}$$

Considering $\delta\in[0,\pi/2]$, we obtain the expression of δ in equation (2.13). The inner radius r can be derived by

$$r=|OP_4|$$
$$=|OP_3|+|P_1P_2|+|P_2O_1|$$
$$=\frac{|P_1P_3|}{\tan\delta}+\frac{|P_2P_5|}{\sin\delta}+\frac{|O_1O_2|\sin\beta'}{\sin\delta}$$
$$=\frac{c}{2\tan\delta}+\frac{c}{2\sin\delta}+\frac{a\sin\beta'}{\sin\delta}$$
$$=\frac{c}{2\tan\delta}+\frac{c\sqrt{1+\tan^2\delta}}{2\tan\delta}+\frac{a\sqrt{1+\tan^2\delta}}{\tan\delta}\frac{\tan\beta'}{\sqrt{1+\tan^2\beta'}}. \tag{A 11}$$

Substituting equations (A 5) and (A 10) into equation (A 11), we can obtain the expression of r in equations (2.10) and (2.12). The inner radius of the flat pattern r_0 can be obtained by simply

substituting $\delta = \delta_0$ and $\beta' = \beta$ into equation (A 11). Specifically, we have

$$\begin{aligned} r_0 &= \frac{c}{2\tan\delta_0} + \frac{c}{2\sin\delta_0} + \frac{a\sin\beta}{\sin\delta_0} \\ &= c \times \frac{\cos\delta_0 + 1}{2\sin\delta_0} + a \times \frac{\sin\beta}{\sin\delta_0}. \end{aligned} \tag{A 12}$$

For the ABO with M unit cells in the radial direction, the outer radius R can be derived by

$$\begin{aligned} R &= |OP_6| + 2M|O_2O_4'| \\ &= |OP_1| + |P_1P_5| + |P_2O_2| + 2M|O_2O_4'| \\ &= \frac{|P_1P_3|}{\sin\delta} + \frac{|P_2P_5|}{\tan\delta} + \frac{|O_1O_2|\sin\alpha'}{\sin\delta} + 2M|O_2O_4|\sin\left(\frac{\eta}{2}\right) \\ &= \frac{c}{2\sin\delta} + \frac{c}{2\tan\delta} + \frac{a\sin\alpha'}{\sin\delta} + 2Md\sin\frac{\eta}{2} \\ &= \frac{c\sqrt{1+\tan^2\delta}}{2\tan\delta} + \frac{c}{2\tan\delta} + \frac{a\sqrt{1+\tan^2\delta}}{\tan\delta}\frac{\tan\alpha'}{\sqrt{1+\tan^2\alpha'}} + \frac{2Mb\sin\alpha}{\sin\beta}\frac{\cos\beta}{\cos\beta'} \\ &= \frac{c\sqrt{1+\tan^2\delta}}{2\tan\delta} + \frac{c}{2\tan\delta} + \frac{a\sqrt{1+\tan^2\delta}}{\tan\delta}\frac{\tan\alpha'}{\sqrt{1+\tan^2\alpha'}} + \frac{2Mb\sin\alpha}{\tan\beta}\sqrt{1+\tan^2\beta'}. \end{aligned} \tag{A 13}$$

For the derivation in equation (A 13), we have applied equations (2.1) and (A 6). Substituting equations (A 1), (A 5) and (A 10) into equation (A 13), we can obtain the expression of R in equations (2.11) and (2.12). The outer radius of the flat pattern R_0 can be obtained by simply substituting $\delta = \delta_0$, $\beta' = \beta$ and $\alpha' = \alpha$ into equation (A 13). Specifically, we have the following derivations:

$$\begin{aligned} R_0 &= \frac{c}{2\sin\delta_0} + \frac{c}{2\tan\delta_0} + \frac{a\sin\alpha}{\sin\delta_0} + \frac{2Mb\sin\alpha}{\sin\beta} \\ &= c \times \frac{\cos\delta_0 + 1}{2\sin\delta_0} + a \times \frac{\sin\alpha}{\sin\delta_0} + 2Mb \times \frac{\sin\alpha}{\sin\beta}. \end{aligned} \tag{A 14}$$

Finally, the expression of height h in equation (2.14) can be derived by

$$h = |O_4O_4'| = |O_3O_3'| = |O_3O_5|\cos\left(\frac{\gamma}{2}\right) = |O_1O_3|\sin\alpha\cos\left(\frac{\gamma}{2}\right) = b\sin\alpha\cos\left(\frac{\gamma}{2}\right). \tag{A 15}$$

Appendix B. Derivation of $\tilde{\gamma}_c$

Substituting the expression of $\tilde{\delta}(\gamma)$ in equation (3.2) to the equation $\tilde{\delta}(\gamma) = 2\pi$, we obtain

$$2N\arctan\left[\frac{\cos(\tilde{\gamma}/2)(\tan\alpha - \tan\beta)}{1 + \cos^2(\tilde{\gamma}/2)\tan\alpha\tan\beta}\right] = 2\pi. \tag{B 1}$$

Equation (B 1) leads to

$$\cos\left(\frac{\tilde{\gamma}}{2}\right) = \frac{H(\alpha,\beta) \pm \sqrt{\Delta(\alpha,\beta,N)}}{\sqrt{\tan\alpha\tan\beta}\tan(\pi/N)}, \tag{B 2}$$

in which the functions $H(\alpha,\beta)$ and $\Delta(\alpha,\beta,N)$ are defined by

$$H(\alpha,\beta) = \frac{\tan\alpha - \tan\beta}{2\sqrt{\tan\alpha\tan\beta}} \quad \text{and} \quad \Delta(\alpha,\beta,N) = [H(\alpha,\beta)]^2 - \tan^2\left(\frac{\pi}{N}\right). \tag{B 3}$$

Considering the range of the variable $\tilde{\gamma} \in [0,\pi]$, we obtain

$$\tilde{\gamma} = \tilde{\gamma}_\pm = 2\arccos\left[\frac{H(\alpha,\beta) \pm \sqrt{\Delta(\alpha,\beta,N)}}{\sqrt{\tan\alpha\tan\beta}\tan(\pi/N)}\right]. \tag{B 4}$$

We need to check the validity of the solutions $\tilde{\gamma}_\pm$. When doing this, two preconditions should be satisfied: $0 < \beta < \alpha < \pi/2$ and $\tilde{\delta}_{\max} \geq 2\pi$. The condition $0 < \beta < \alpha < \pi/2$ guarantees the angles

α and β can generate a non-degenerate ABO configuration, which also yields the following relationships:

$$\tan\alpha - \tan\beta > 0 \quad \text{and} \quad 0 < \alpha - \beta < \frac{\pi}{2}. \tag{B 5}$$

The condition $\tilde{\delta}_{\max} \geq 2\pi$ guarantees the equation $\tilde{\delta}(\gamma) = 2\pi$ has at least one valid solution. According to equation (3.5), the condition $\tilde{\delta}_{\max} \geq 2\pi$ reads

$$\tilde{\delta}_{\max} \geq 2\pi \;\Leftrightarrow\; \begin{cases} \alpha - \beta \geq \dfrac{\pi}{N}, & \text{if } 0 < \alpha + \beta \leq \dfrac{\pi}{2}, \\ H(\alpha,\beta) \geq \tan(\dfrac{\pi}{N}), & \text{if } \dfrac{\pi}{2} < \alpha + \beta < \pi. \end{cases} \tag{B 6}$$

The following relationships will be useful:

$$\left.\begin{aligned} 0 < \alpha, \beta < \frac{\pi}{2} \text{ and } 0 < \alpha + \beta \leq \frac{\pi}{2} \Rightarrow 0 < \tan\alpha\tan\beta \leq 1 \\ \text{and} \quad 0 < \alpha, \beta < \frac{\pi}{2} \text{ and } \frac{\pi}{2} < \alpha + \beta < \pi \Rightarrow \tan\alpha\tan\beta > 1. \end{aligned}\right\} \tag{B 7}$$

For conciseness, we will not specifically point them out when we use the relationships (B 5) and (B 7) in the following text. To begin with, we check the sign of the function $\Delta(\alpha, \beta, N)$. It is useful to rewrite $\Delta(\alpha, \beta, N)$ as the following forms:

$$\Delta(\alpha,\beta,N) = \frac{\tan(\alpha-\beta) - \tan(\pi/N)}{\cot(\pi/N)/(1+\tan\alpha\tan\beta)} + \left[H(\alpha,\beta) - \sqrt{\tan\alpha\tan\beta}\tan\left(\frac{\pi}{N}\right)\right]^2 \tag{B 8}$$

and

$$\Delta(\alpha,\beta,N) = \frac{H(\alpha,\beta) - \tan(\pi/N)}{\cot(\pi/N)/2} + \left[H(\alpha,\beta) - \tan\left(\frac{\pi}{N}\right)\right]^2. \tag{B 9}$$

When $0 < \alpha + \beta \leq \pi/2$, the condition (B 6) is $\alpha - \beta \geq \pi/N$, which leads to $\Delta(\alpha, \beta, N) \geq 0$ according to equation (B 8). When $\pi/2 < \alpha + \beta < \pi$, the condition (B 6) is $H(\alpha, \beta) \geq \tan(\pi/N)$, which leads to $\Delta(\alpha, \beta, N) \geq 0$ according to equation (B 9). Thus, the square root operation $\sqrt{\Delta(\alpha, \beta, N)}$ always gets a real number. Next, we consider the range of the folding angle $\tilde{\gamma} \in [0, \pi]$. This means the valid solutions $\tilde{\gamma}_\pm$ should satisfy $0 \leq \cos(\tilde{\gamma}_\pm/2) \leq 1$, in which $\cos(\tilde{\gamma}_\pm/2)$ is given in equation (B 2). For the inequalities on the left-hand side, we know $\cos(\tilde{\gamma}_\pm/2) \geq 0$ always holds true, which is due to $H(\alpha, \beta) > \sqrt{\Delta(\alpha, \beta, N)} > 0$ based on equation (B 3). For the right-hand side, we deal with $\cos(\tilde{\gamma}_-/2) \leq 1$ and $\cos(\tilde{\gamma}_+/2) \leq 1$ separately. First, we check the constraint $\cos(\tilde{\gamma}_-/2) \leq 1$. When $0 < \alpha + \beta \leq \pi/2$, the condition (B 6) is $\alpha - \beta \geq \pi/N$. Based on equations (B 4) and (B 8), we have

$$\cos\left(\frac{\tilde{\gamma}_-}{2}\right) = \frac{H(\alpha,\beta) - \sqrt{\Delta(\alpha,\beta,N)}}{\sqrt{\tan\alpha\tan\beta}\tan(\pi/N)} \leq 1. \tag{B 10}$$

The equality $\cos(\tilde{\gamma}_-/2) = 1$ holds if and only if $\alpha - \beta = \pi/N$. In this case, we have $\tilde{\gamma}_- = 0$. When $\pi/2 < \alpha + \beta < \pi$, the condition (B 6) is $H(\alpha, \beta) \geq \tan(\pi/N)$. Based on equations (B 4) and (B 9), we have

$$\cos\left(\frac{\tilde{\gamma}_-}{2}\right) = \frac{H(\alpha,\beta) - \sqrt{\Delta(\alpha,\beta,N)}}{\sqrt{\tan\alpha\tan\beta}\tan(\pi/N)} \leq \frac{1}{\sqrt{\tan\alpha\tan\beta}} < 1. \tag{B 11}$$

The strict inequality $\cos(\tilde{\gamma}_-/2) < 1$ implies $\tilde{\gamma}_- > 0$ for $\pi/2 < \alpha + \beta < \pi$. The above derivations prove that $\tilde{\gamma}_-$ is always a valid solution to the equation $\tilde{\delta}(\gamma) = 2\pi$ as long as the two preconditions $0 < \alpha < \beta < \pi/2$ and $\tilde{\delta}_{\max} \geq 2\pi$ are satisfied. Second, we check the constraint $\cos(\tilde{\gamma}_+/2) \leq 1$. We rewrite $H(\alpha, \beta)$ as

$$H(\alpha,\beta) = \frac{1+\tan\alpha\tan\beta}{2\sqrt{\tan\alpha\tan\beta}}\tan(\alpha-\beta), \tag{B 12}$$

and rewrite $\Delta(\alpha, \beta, N)$ as

$$\Delta(\alpha,\beta,N) = \frac{(1+\tan\alpha\tan\beta)^2}{4\tan\alpha\tan\beta}\left[\tan^2(\alpha-\beta) - \tan^2\left(\frac{\pi}{N}\right)\right] + \left[\frac{1-\tan\alpha\tan\beta}{2\sqrt{\tan\alpha\tan\beta}}\tan\left(\frac{\pi}{N}\right)\right]^2. \tag{B 13}$$

When $0 < \alpha + \beta \leq \pi/2$, the condition (B 6) gives $\alpha - \beta \geq \pi/N$. equations (B 4), (B 12) and (B 13) lead to

$$\cos\left(\frac{\tilde{\gamma}_+}{2}\right) = \frac{H(\alpha,\beta) + \sqrt{\Delta(\alpha,\beta,N)}}{\sqrt{\tan\alpha\tan\beta}\tan(\pi/N)} \geq \frac{1}{\tan\alpha\tan\beta} \geq 1. \tag{B 14}$$

The equality $\cos(\tilde{\gamma}_+/2) = 1$ holds if and only if $\alpha - \beta = \pi/N$ and $\alpha + \beta = \pi/2$. In this case, we have $\tilde{\gamma}_+ = \tilde{\gamma}_- = 0$. Otherwise, the solution $\tilde{\gamma}_+$ is not valid. When $\pi/2 < \alpha + \beta < \pi$, the condition (B 6) gives $H(\alpha,\beta) \geq \tan(\pi/N)$. The expression of $H(\alpha,\beta)$ given in equation (B 3) implies

$$H(\alpha,\beta) \geq \tan(\alpha - \beta). \tag{B 15}$$

Therefore, we can further consider two different situations: $\alpha - \beta > \pi/N$ and $\alpha - \beta \leq \pi/N$. If $\alpha - \beta > \pi/N$, equations (B 4), (B 12) and (B 13) lead to

$$\cos\left(\frac{\tilde{\gamma}_+}{2}\right) = \frac{H(\alpha,\beta) + \sqrt{\Delta(\alpha,\beta,N)}}{\sqrt{\tan\alpha\tan\beta}\tan(\pi/N)} > 1, \tag{B 16}$$

which indicates $\tilde{\gamma}_+$ is not a valid solution. If $\alpha - \beta \leq \pi/N$, equation (B 4), (B 12) and (B 13) lead to

$$\cos\left(\frac{\tilde{\gamma}_+}{2}\right) = \frac{H(\alpha,\beta) + \sqrt{\Delta(\alpha,\beta,N)}}{\sqrt{\tan\alpha\tan\beta}\tan(\pi/N)} \leq 1, \tag{B 17}$$

which indicates $\tilde{\gamma}_+$ is a valid solution. Specifically, when $\alpha - \beta = \pi/N$, we have $\tilde{\gamma}_+ = 0$ and $\tilde{\gamma}_- > 0$. When $\alpha - \beta < \pi/N$, we have $0 < \tilde{\gamma}_+ \leq \tilde{\gamma}_-$. The double solution $\tilde{\gamma}_+ = \tilde{\gamma}_-$ arises if $H(\alpha,\beta) = \tan(\pi/N)$. In this case, we have $\tilde{\gamma}_+ = \tilde{\gamma}_- = \tilde{\gamma}^\star = 2\arccos(1/\sqrt{\tan\alpha\tan\beta})$. Altogether, we can write the solutions of the equation $\tilde{\delta}(\tilde{\gamma})|_{\tilde{\gamma}=\tilde{\gamma}_c} = 2\pi$ as

$$\tilde{\gamma}_c = \begin{cases} 0, & \text{if } 0 < \alpha+\beta \leq \dfrac{\pi}{2} \text{ and } \alpha-\beta = \dfrac{\pi}{N}, \\ \tilde{\gamma}^\star, & \text{if } \dfrac{\pi}{2} < \alpha+\beta < \pi \text{ and } \alpha-\beta < \dfrac{\pi}{N} \text{ and } H(\alpha,\beta) = \tan\left(\dfrac{\pi}{N}\right), \\ \tilde{\gamma}_+ \text{ or } \tilde{\gamma}_-, & \text{if } \dfrac{\pi}{2} < \alpha+\beta < \pi \text{ and } \alpha-\beta < \dfrac{\pi}{N} \text{ and } H(\alpha,\beta) > \tan\left(\dfrac{\pi}{N}\right), \\ 0 \text{ or } \tilde{\gamma}_-, & \text{if } \dfrac{\pi}{2} < \alpha+\beta < \pi \text{ and } \alpha-\beta = \dfrac{\pi}{N} \text{ and } H(\alpha,\beta) \geq \tan\left(\dfrac{\pi}{N}\right), \\ \tilde{\gamma}_-, & \text{if } \alpha-\beta > \dfrac{\pi}{N}. \end{cases} \tag{B 18}$$

In equations (B 18) and (3.11), the subdomains of the piecewise expression of $\tilde{\gamma}_c$ are not in the same forms. Now we prove the partition of subdomains in equation (B 18) are equivalent to that in equation (3.11). First, we prove the following equivalences:

$$\left.\begin{aligned} &H(\alpha,\beta) = \tan(\pi/N) \Leftrightarrow L(\alpha,\beta) = T(N) \\ \text{and} \quad &H(\alpha,\beta) > \tan\left(\frac{\pi}{N}\right) \Leftrightarrow L(\alpha,\beta) > T(N), \end{aligned}\right\} \tag{B 19}$$

in which the functions $L(\alpha,\beta)$ and $T(N)$ are given in equation (3.8). To do this, we recall the function $H(\alpha,\beta)$ can be written as $H = [L(\alpha,\beta) - 1/L(\alpha,\beta)]/2$. By solving $[L(\alpha,\beta) - 1/L(\alpha,\beta)]/2 = \tan(\pi/N)$, we obtain $L(\alpha,\beta) = [\sin(\pi/N) + 1]/\cos(\pi/N) = T(N)$. Then the equivalences (B 19) can be proved by the fact that $H(\alpha,\beta)$ is monotonically increasing with $L(\alpha,\beta)$ increasing. Second, we have the following relationship

$$\alpha - \beta = \frac{\pi}{N} \Rightarrow H(\alpha,\beta) \geq \tan\left(\frac{\pi}{N}\right). \tag{B 20}$$

This is obvious according to equation (B 15). Therefore, equation (B 18) is equivalent to equation (3.11). Finally, equations (B 6) and (B 19) lead to equation (3.10).

References

1. Vinson JR. 2001 Sandwich structures. *Appl. Mech. Rev.* **54**, 201–214. (doi:10.1115/1.3097295)

2. Birman V, Kardomateas GA. 2018 Review of current trends in research and applications of sandwich structures. *Compos. Part B: Eng.* **142**, 221–240. (doi:10.1016/j.compositesb.2018.01.027)
3. Herrmann AS, Zahlen PC, Zuardy I. 2005 Sandwich structures technology in commercial aviation. In *Sandwich Structures 7: Advancing with Sandwich Structures and Materials, Proc. of the 7th Int. Conf. on Sandwich Structures, Aalborg, Denmark, 29–31 August 2005* (eds O Thomsen, E Bozhevolnaya, A Lyckegaard), pp. 13–26. Dordrecht, The Netherlands: Springer. (doi:10.1007/1-4020-3848-8_2)
4. Castanie B, Bouvet C, Ginot M. 2020 Review of composite sandwich structure in aeronautic applications. *Compos. Part C: Open Access* **1**, 100004. (doi:10.1016/j.jcomc.2020.100004)
5. Klett Y, Drechsler K, Wang-Iverson P, Lang R, Yim M. 2011 Designing technical tessellations. In *Origami 5: Proc. of the 5th Int. Meeting of Origami Science, Mathematics, and Education, Singapore, 13–17 July 2010* (eds P Wang-Iverson, RJ Lang, M Yim), pp. 305–322. Boca Raton: CRC Press.
6. Rapp EG. 1960 Sandwich-type structural element. US Patent 2963128.
7. Miura K. 1972 Zeta-core sandwich–Its concept and realization. ISAS Report 480, Institute of Space and Aeronautical Science, University of Tokyo.
8. Klett Y, Drechsler K, Kolax M, Wentzel H, Kehrle R. 2007 Design of multifunctional folded core structures for aerospace sandwich applications. In *Proc. of the 1st CEAS European Air and Space Conf., Berlin, 10–13 September 2007,* pp. 903–908.
9. Johnson AF. 2008 Novel hybrid structural core sandwich materials for aircraft applications. In *Proc. of the 11th Euro-Japanese Symp. on Composite Materials*, Porto, Portugal, 9–11 September 2008. Tokyo, JSCM.
10. Heimbs S. 2013 Foldcore sandwich structures and their impact behaviour: An overview. In *Dynamic Failure of Composite and Sandwich Structures* (eds S Abrate, B Castanié, YDS Rajapakse), pp. 491–544. Dordrecht, The Netherlands: Springer.
11. CELPACT. 2006–2009 Cellular structures for impact performance. EU Research Project, FP6-031038.
12. Heimbs S, Kilchert S, Fischer S, Klaus M, Baranger E. 2009 Sandwich structures with folded core: mechanical modeling and impact simulations. In *Proc. of the SAMPE Europe Int. Conf. (SEICO-09), Paris, 23–25 March 2009*, pp. 324–331. Red Hook, NY: Curran Associates.
13. Fischer S, Heimbs S, Kilchert S, Klaus M, Cluzel C. 2009 Sandwich structures with folded core: manufacturing and mechanical behavior. In *Proc. of the SAMPE Europe Int. Conf. (SEICO-09), Paris, 23–25 March 2009,* pp. 256–263.
14. Miura K. 1985 Method of packaging and deployment of large membranes in space. ISAS Report 618, Institute of Space and Aeronautical Science, University of Tokyo.
15. Filipov ET, Tachi T, Paulino GH. 2015 Origami tubes assembled into stiff, yet reconfigurable structures and metamaterials. *Proc. Natl Acad. Sci. USA* **112**, 12 321–12 326. (doi:10.1073/pnas.1509465112)
16. Liu Q, Wang W, Reynolds MF, Cao MC, Miskin MZ, Arias TA, Muller DA, McEuen PL, Cohen I. 2021 Micrometer-sized electrically programmable shape-memory actuators for low-power microrobotics. *Sci. Rob.* **6**, eabe6663. (doi:10.1126/scirobotics.abe6663)
17. Kim W, Byun J, Kim JK, Choi WY, Jakobsen K, Jakobsen J, Lee DY, Cho KJ. 2019 Bioinspired dual-morphing stretchable origami. *Sci. Rob.* **4**, eaay3493. (doi:10.1126/scirobotics.aay3493)
18. Tang R, Huang H, Tu H, Liang H, Liang M, Song Z, Xu Y, Jiang H, Yu H. 2014 Origami-enabled deformable silicon solar cells. *Appl. Phys. Lett.* **104**, 083501. (doi:10.1063/1.4866145)
19. Nauroze SA, Novelino LS, Tentzeris MM, Paulino GH. 2018 Continuous-range tunable multilayer frequency-selective surfaces using origami and inkjet printing. *Proc. Natl Acad. Sci. USA* **115**, 13 210–13 215. (doi:10.1073/pnas.1812486115)
20. Gattas J, You Z. 2014 Quasi-static impact of indented foldcores. *Int. J. Impact Eng.* **73**, 15–29. (doi:10.1016/j.ijimpeng.2014.06.001)
21. Xiang X, You Z, Lu G. 2018 Rectangular sandwich plates with Miura-ori folded core under quasi-static loadings. *Compos. Struct.* **195**, 359–374. (doi:10.1016/j.compstruct.2018.04.084)
22. Wang F, Gong H, Chen X, Chen C. 2016 Folding to curved surfaces: a generalized design method and mechanics of origami-based cylindrical structures. *Sci. Rep.* **6**, 33312. (doi:10.1038/srep33312)
23. Hu Y, Liang H, Duan H. 2019 Design of cylindrical and axisymmetric origami structures based on generalized Miura-ori cell. *J. Mech. Rob.* **11**, 051004. (doi:10.1115/1.4043800)

24. Song K, Zhou X, Zang S, Wang H, You Z. 2017 Design of rigid-foldable doubly curved origami tessellations based on trapezoidal crease patterns. *Proc. R. Soc. A* **473**, 20170016. (doi:10.1098/rspa.2017.0016)
25. Dang X, Lu L, Duan H, Wang J. 2022 Deployment kinematics of axisymmetric Miura origami: unit cells, tessellations, and stacked metamaterials. *Int. J. Mech. Sci.* **232**, 107615. (doi:10.1016/j.ijmecsci.2022.107615)
26. Sareh P, Guest S. 2015a Design of isomorphic symmetric descendants of the Miura-ori. *Smart Mater. Struct.* **24**, 085001. (doi:10.1088/0964-1726/24/8/085001)
27. Sareh P, Guest S. 2015b Design of non-isomorphic symmetric descendants of the Miura-ori. *Smart Mater. Struct.* **24**, 085002. (doi:10.1088/0964-1726/24/8/085002)
28. Gattas JM, You Z. 2014 Miura-base rigid origami: parametrizations of curved-crease geometries. *J. Mech. Des.* **136**, 121404. (doi:10.1115/1.4028532)
29. Zhou X, Zang S, You Z. 2016 Origami mechanical metamaterials based on the Miura-derivative fold patterns. *Proc. R. Soc. A* **472**, 20160361. (doi:10.1098/rspa.2016.0361)
30. Liu K, Paulino GH. 2017 Nonlinear mechanics of non-rigid origami: an efficient computational approach. *Proc. R. Soc. A* **473**, 20170348. (doi:10.1098/rspa.2017.0348)
31. Liu K, Paulino GH. 2018 Highly efficient nonlinear structural analysis of origami assemblages using the MERLIN2 software. In *Origami 7: Proc. of the 7th Int. Meeting on Origami in Science, Mathematics, and Education, Oxford, 5–7 September 2018* (eds RJ Lang, M Bolitho, Z You), pp. 1167–1182. Hertfordshire: Tarquin.
32. Liu K, Novelino LS, Gardoni P, Paulino GH. 2020 Big influence of small random imperfections in origami-based metamaterials. *Proc. R. Soc. A* **476**, 20200236. (doi:10.1098/rspa.2020.0236)
33. Schenk M, Allwood J, Guest S. 2011 Cold gas-pressure folding of Miura-ori sheets. In *Proc. of the 10th Int. Conf. on Technology of Plasticity* (*ICTP 2011*), *Aachen, Germany, 25–30 September 2011* (eds G Hirt, AE Tekkaya), pp. 459–464. Düsseldorf: Verl. Stahleisen GmbH.
34. Filipov E, Liu K, Tachi T, Schenk M, Paulino G. 2017 Bar and hinge models for scalable analysis of origami. *Int. J. Solids Struct.* **124**, 26–45. (doi:10.1016/j.ijsolstr.2017.05.028)
35. Timoshenko SP, Gere JM. 2009 *Theory of elastic stability*, 2nd edn. New York, NY: Dover Publications.
36. Dang X, Paulino GH. 2024 Axisymmetric blockfold origami: a non-flat-foldable Miura variant with self-locking mechanisms and enhanced stiffness. Figshare. (doi:10.6084/m9.figshare.c.7132041)